Global Barotropic Tide Modeling Using Inline Self-Attraction and Loading in MPAS-Ocean

Kristin N. Barton[1] , Nairita Pal[2], Steven R. Brus[3], Mark R. Petersen[2] , Brian K. Arbic[4] , Darren Engwirda[2] , Andrew F. Roberts[2] , Joannes J. Westerink[5], Damrongsak Wirasaet[5], and Michael Schindelegger[6]

[1]Department of Physics, University of Michigan, Ann Arbor, MI, USA, [2]Los Alamos National Laboratory, Los Alamos, NM, USA, [3]Mathematics and Computer Science Division, Argonne National Laboratory, Lemont, IL, USA, [4]Department of Earth and Environmental Sciences, University of Michigan, Ann Arbor, MI, USA, [5]Department of Civil and Environmental Engineering and Earth Sciences, University of Notre Dame, Notre Dame, IN, USA, [6]Institute of Geodesy and Geoinformation, University of Bonn, Bonn, Germany

Abstract We examine ocean tides in the barotropic version of the Model for Prediction Across Scales (MPAS-Ocean), the ocean component of the Department of Energy Earth system model. We focus on four factors that affect tidal accuracy: self-attraction and loading (SAL), model resolution, details of the underlying bathymetry, and parameterized topographic wave drag. The SAL term accounts for the tidal loading of Earth's crust and the self-gravitation of the ocean and the load-deformed Earth. A common method for calculating SAL is to decompose mass anomalies into their spherical harmonic constituents. Here, we compare a scalar SAL approximation versus an inline SAL using a fast spherical harmonic transform package. Wave drag accounts for energy lost by breaking internal tides that are produced by barotropic tidal flow over topographic features. We compare a series of successively finer quasi-uniform resolution meshes (62.9, 31.5, 15.7, and 7.87 km) to a variable resolution (45 to 5 km) configuration. We ran MPAS-Ocean in a single-layer barotropic mode forced by five tidal constituents. The 45 to 5 km variable resolution mesh obtained the best total root-mean-square error (5.4 cm) for the deep ocean (>1,000 m) M_2 tide compared to TPXO8 and ran twice as fast as the quasi-uniform 8 km mesh, which had an error of 5.8 cm. This error is comparable to those found in other forward (non-assimilative) ocean tide models. In future work, we plan to use MPAS-Ocean to study tidal interactions with other Earth system components, and the tidal response to climate change.

Plain Language Summary Over the next century, climate change impacts on coastal regions will include floods, droughts, erosion, and severe weather events. The Department of Energy (DoE) is funding the Integrated Coastal Modeling Project to understand these potential risks better. In this paper, we implement tides in the DoE ocean model. Tides themselves respond to climate change, altering coastal flooding risk assessments. We explore the sensitivity of tides to model resolution (the spacing of model gridpoints), ocean-floor topography, and the so-called "self-attraction and loading" (SAL) effect. Self-attraction and loading occurs as the mass of water in a location fluctuates, causing a deformation of the Earth's crust and changes in the gravitational potential, which must be accounted for when modeling tides. We present a computationally efficient method of calculating the SAL effects and show that it is more accurate than other commonly used approximations. In future work we will examine interactions of tides with other components of the climate system, including sea ice, floating ice shelves, rivers, and current systems.

1. Introduction

Tides are an integral and dynamic component of the Earth system. According to the IPCC Special Report for Oceans and Cryosphere in a Changing Climate, "it is *very likely* that the majority of coastal regions will experience statistically significant changes in tidal amplitudes over the course of the 21st century" (Bindoff et al., 2019). Additionally, the report concluded with "*high confidence*" that tides are one of several local processes essential to predicting future extreme sea level events (Oppenheimer et al., 2019). Coastal tide gauge records point to changes in tidal amplitudes by as much as 1%–2% per decade (Flick et al., 2003; Müller et al., 2011; Ray, 2006). In some locations, the secular changes in tidal amplitudes are of comparable magnitude to changes in mean sea level (Jay, 2009). There are a number of processes that affect observed tides in a particular region, from long-term Earth system processes (such as tectonic motion) to shorter-term processes which could have impacts over the

next century (Haigh et al., 2020). For example, mean sea-level rise, shoreline position, or the depth of estuaries can influence the geometry of the local region such that tidal resonance is altered and amphidromic points shift spatially. Meanwhile, seabed roughness, river flow, sea ice coverage, or ocean stratification, can lead to changes in the frictional dissipation and energy exchange of the tides (Haigh et al., 2020). These non-astronomical effects are the reason for efforts now to include changes in tides as a factor in assessing flood risks in a changing climate (Haigh et al., 2020; Jay, 2009). In order to model and predict tidal changes and their impacts in a changing climate, it is desirable to simulate tides within an Earth system model.

Historically, tide modeling and climate modeling have been performed separately. In relatively recent efforts, the two types of modeling have been performed concurrently (Arbic et al., 2018). Tide gauges have been used for centuries to determine tidal amplitudes and phases at specific locations, but as computational methods became more feasible, work began on developing tide models that would allow tidal amplitude and phases to be estimated at any point in the ocean (Pekeris & Accad, 1969). The resolution and accuracy of these early barotropic tide models increased throughout the late twentieth century with the help of increased computational power and assimilation from satellite altimeter data (Dushaw et al., 1997; Hendershott, 1972; Le Provost et al., 1994; Parke & Hendershott, 1980; Ray, 1993; Schwiderski, 1979; Shum et al., 1997). Conversely, baroclinic climate models have historically excluded explicit tide calculations due to computational constraints and the use of large time steps for long-term simulations. Early 3-D ocean models used a "rigid-lid" assumption to remove barotropic gravity waves, thus not permitting tides at all (Bryan, 1969; Griffies et al., 2000). The first studies to include tides in a baroclinic model were performed at regional scales (Cummins & Oey, 1997; Kang et al., 2000; Merrifield et al., 2001). The first global simulations of baroclinic tides (Arbic et al., 2004; Simmons et al., 2004) included only tidal forcing. Over the past decade, several ocean general circulation models have begun incorporating tides (Arbic et al., 2010, 2018; Müller et al., 2012; Rocha et al., 2016; Waterhouse et al., 2014), allowing for investigations into interactions of barotropic and internal tides with mesoscale eddies and other components of the Earth system.

Several factors must be examined and accounted for in global tide models, including self-attraction and loading (SAL), model resolution, the underlying bathymetric data set, and parameterized topographic wave drag. SAL accounts for a combination of effects: the deformation of the Earth's crust due to mass loading and the self-gravitation of the load-deformed Earth as well as of the ocean tide itself (Hendershott, 1972). Self-attraction and loading can change tidal amplitudes to first-order, up to 20% in some regions, and also significantly impacts tidal phases and amphidromic points (Gordeev et al., 1977). Full calculation of SAL calls for convolution of tidal elevation with a proper Green's function or a multiplication with load Love numbers in the spectral—i.e., spherical harmonic—domain (Ray, 1998). Early attempts to calculate SAL using spherical harmonics proved expensive (Stepanov & Hughes, 2004), so ocean tide models have often employed cheaper methods, such as a scalar approximation (in which the SAL is approximated locally by a constant factor multiplied by the tidal elevation), an iterative method, or the use of SAL fields drawn from other sources. The scalar approximation fails to preserve the scale-dependent, spatially smoothing behavior of the SAL and can be particularly unreliable in shelf areas where tidal length scales are much smaller than in the open ocean (Ray, 1998). The iterative method is tedious to employ and relies on intermediate harmonic analysis, meaning that non-periodic self-attraction and loading effects, such as those associated with storm surges, cannot be easily accounted for. Reading in a data set for SAL can improve the accuracy of modeled tides in the present-day, but is not appropriate for the prediction of tides in a future world where tides and other climate system components will be different. Motivated by these points and by recent works incorporating SAL in various hydrodynamic frameworks (Schindelegger et al., 2018; Shihora et al., 2022; Vinogradova et al., 2015), we choose to implement a full inline calculation of SAL for tides. The model we use is the oceanic component of the Department of Energy (DOE) Energy Exascale Earth System Model (E3SM)—namely, the ocean Model for Prediction Across Scales (MPAS-Ocean).

This paper represents a first step toward embedding tides within MPAS-Ocean. We evaluate MPAS-Ocean as a barotropic tide model in preparation for including tides in full baroclinic simulations. We demonstrate the feasibility of implementing a full inline calculation of SAL using the barotropic configuration. Furthermore, we compare tidal sensitivity to different bathymetric products, different resolutions, and parameterized topographic wave drag. Sensitivity to bathymetry in tidal simulations has been demonstrated previously and can be improved with high-quality regional patching (Blakely et al., 2022; Lyard et al., 2021). Convergence of tidal errors with increasing model grid resolution has been explored in, for example, Egbert et al. (2004), Arbic et al. (2008), and

Pringle et al. (2021). A parameterized topographic wave drag accounts for the energy dissipation that occurs when internal tides are generated from the tidal flow over rough topography in the presence of stratification. The importance of including this term in barotropic tidal simulations has been discussed in many papers (Arbic et al., 2004, 2008; Blakely et al., 2022; Egbert et al., 2004; Jayne & St. Laurent, 2001). Finally, we expect the inclusion of a full SAL calculation to increase the computational time of the simulations, as has been shown in previous implementations (Schindelegger et al., 2018; Shihora et al., 2022). We end with an examination of the computational cost incurred by our SAL calculation and compare performance on the various resolution meshes used in the study.

2. Methods and Implementation

2.1. Model Description

The Model for Prediction Across Scales, or MPAS, integrates a variety of geophysical fluid dynamics models on unstructured meshes (Golaz et al., 2019; Petersen et al., 2019; Ringler et al., 2013). MPAS contains various dynamical cores, each of which contains a specific implementation of a physical system (e.g., atmosphere, sea ice, etc.). We implement tides in the ocean core, MPAS-Ocean. The model is based on unstructured, Voronoi-type tessellations supporting variable resolution, allowing for a range of spatial length scales to be captured in a single simulation. A variable resolution unstructured mesh allows for a detailed representation of some regions (e.g., coastlines) while reducing overall computational cost through the use of lower resolutions in regions with larger length scales.

For the purpose of evaluating tides in MPAS-Ocean, we have modified the model to run in a two-dimensional (2-D) barotropic mode. The governing equations include a momentum equation in a vector-invariant form and a layer thickness equation.

$$\frac{\partial \mathbf{u}}{\partial t} + (\nabla \times \mathbf{u} + f\mathbf{k}) \times \mathbf{u} = -\nabla K - g\nabla(\eta - \eta_{EQ} - \eta_{SAL}) - \chi \frac{C\mathbf{u}}{H} - \frac{C_D |\mathbf{u}| \mathbf{u}}{H}, \tag{1}$$

$$\frac{\partial h}{\partial t} + \nabla \cdot (h\mathbf{u}) = 0, \tag{2}$$

where $\mathbf{u}$ represents the depth-averaged horizontal velocity, t is the time coordinate, f is the Coriolis parameter, $\mathbf{k}$ is the vertical unit vector, $K = |\mathbf{u}|^2/2$ is the kinetic energy, g is the gravitational acceleration constant, η is the sea-surface height relative to the moving bed, henceforth called SSH, η_{EQ} is the equilibrium tide, η_{SAL} is the perturbation of tidal elevations due to SAL, χ is a tunable scalar dimensionless wave drag coefficient, $\frac{C}{h}$ is a topographic wave drag time scale, H is the resting depth of the ocean, and h is the total ocean thickness such that $H + \eta = h$. The full form of the drag terms in Equation 1 would use the total thickness h, but our implementation uses the linearized version with the resting depth H. In addition, $\frac{H}{C}$ is read in from the variable `rinv` from the HyCOM file `jsl_lim24_inv_hrs.nc`, where the original calculation is described in Buijsman et al. (2016). C_D is a log-law based drag model, evaluated according to Equation 3 where $\kappa = 0.4$ is the von Karman constant (Von Kármán, 1931), $z_0 = 0.001$ is the roughness parameter and H is the ocean resting thickness. The minimum and maximum functions constrain C_D to the range $[0.0025, 0.1]$.

$$C_D = \max\left[0.0025, \min\left[0.1, \left(\frac{\kappa}{\ln\left(\frac{H}{2z_0}\right)}\right)^2\right]\right] \tag{3}$$

MPAS-Ocean retains the capability to be run with multiple layers with tides and SAL for future investigations, but only the single-layer barotropic model is used in this study. The multi-layer baroclinic model would additionally include three-dimensional tracer equations for temperature and salinity, vertical advection and diffusion terms on all equations, and the computation of density from the equation of state for seawater and pressure at each layer from the hydrostatic equation.

Tidal forcing is implemented by adding a SSH perturbation, η_{EQ}, into the pressure gradient operator.

$$\eta_{EQsd,c} = A_c f_c(t_{ref}) L \cos^2(\phi) \cos\left[\omega_c(t - t_{ref}) + \chi_c(t_{ref}) + \nu_c(t_{ref}) + 2\lambda\right] \tag{4}$$

$$\eta_{EQd,c} = A_c f_c(t_{ref}) L \sin(2\phi) \cos\left[\omega_c(t - t_{ref}) + \chi_c(t_{ref}) + \nu_c(t_{ref}) + \lambda\right] \tag{5}$$

These terms are valid for semidiurnal (sd) and diurnal (d) tidal constituents (Arbic et al., 2018). The total forcing comes from summing over each of the constituents, c. Here A and ω are the forcing amplitude and frequency, respectively, dependent on the tidal constituent, t_{ref} is a specified reference time, t is time, ϕ is latitude, λ is longitude, $\chi(t_{ref})$ is an astronomical argument accounting for the constituent's phase due to astronomical positions of the Moon and/or Sun, and $f(t_{ref})$ and $\nu(t_{ref})$ are amplitude and phase nodal factors accounting for small known astronomical modulations in the tidal forcing. $L = 1 + k_2 - h_2$ is a combination of body tide Love numbers that account for changes in the gravitational potential (k_2) due to deformation of the Earth's crust and mantle from tidal forcing (h_2).

2.2. Self-Attraction and Loading

SAL is implemented as additional body force via the SSH gradient term in Equation 1. We express the inline SAL for tides in terms of the spherical harmonic decomposition of the SSH (Hendershott, 1972),

$$\eta_{SAL} = \sum_n \frac{3\rho_0}{\rho_{earth}(2n+1)} \left(1 + k'_n - h'_n\right) \eta_n, \tag{6}$$

where each spherical harmonic SSH term η_n is multiplied by a scalar coefficient. Here $\rho_0 = 1035 \frac{kg}{m^3}$ is the average density of seawater, $\rho_{earth} = 5517 \frac{kg}{m^3}$ is the average density of the solid Earth, and the multiplicative term $(1 + k'_n - h'_n)$ represents load Love numbers (obtained from Wang et al. (2012)) corresponding to physical effects of SAL. The "1", k'_n, and h'_n terms account for gravitational self-attraction of the ocean, gravitational self-attraction of the deformed solid Earth, and deformation due to loading of the solid Earth respectively. However, the usage of SSH for calculating SAL is only appropriate for tides and wind-driven barotropic motions. For other motions one must use bottom pressure anomalies.

Before this work, SAL was implemented in MPAS-Ocean via the scalar approximation (Accad & Pekeris, 1978; Ray, 1998),

$$\eta_{SAL} = \beta\eta, \tag{7}$$

where η is the SSH prior to alterations, and $\beta = 0.09$ is a scalar parameter used to approximate the influence of SAL. This approximation is a computationally inexpensive method that is sufficiently accurate for many cases. However, it does not capture the spatial dependence and large-scale smoothing of the full calculation (Figure 1).

We evaluate Equation 6 using the fast spherical harmonics transform package, SHTns (Schaeffer, 2013). This package can only be run on a single node with shared memory, not across nodes with a message passing interface (MPI). In contrast, MPAS-Ocean typically runs on hundreds of nodes using MPI. Further, the input data must be arranged on a Gaussian grid, because SHTns takes advantage of the geometry of this grid (i.e., the latitudes are arranged at zeros of Legendre polynomials) to perform faster transforms. To use SHTns within MPAS-Ocean, we first gather the distributed SSH field to a single head node before remapping the data onto the Gaussian grid. The remapped data can then be transformed into spherical harmonics, where η_{SAL} is easily calculated by multiplying the harmonic coefficients by the known load Love numbers. Finally, the process is performed in reverse as η_{SAL} is transformed into a spatial field on the Gaussian grid, remapped onto the MPAS mesh, and sent back out to the nodes (Figure 2). For each of the quasi-uniform meshes, the Gaussian grid resolution was chosen to match the mesh resolution at the equator. For the variable resolution mesh, the Gaussian grid resolution is equal to the minimum resolution of the mesh, or 5 km. The spherical harmonic order cutoff is determined by the number of latitudes in the Gaussian grid according to Equation 8, where l_{max} is the maximum degree, m_{max} is the maximum order, and $nlat$ is the number of latitudes in the Gaussian grid.

$$l_{max} = \text{integer}\left(\frac{nlat}{2}\right) - 1$$
$$m_{max} = l_{max} \tag{8}$$
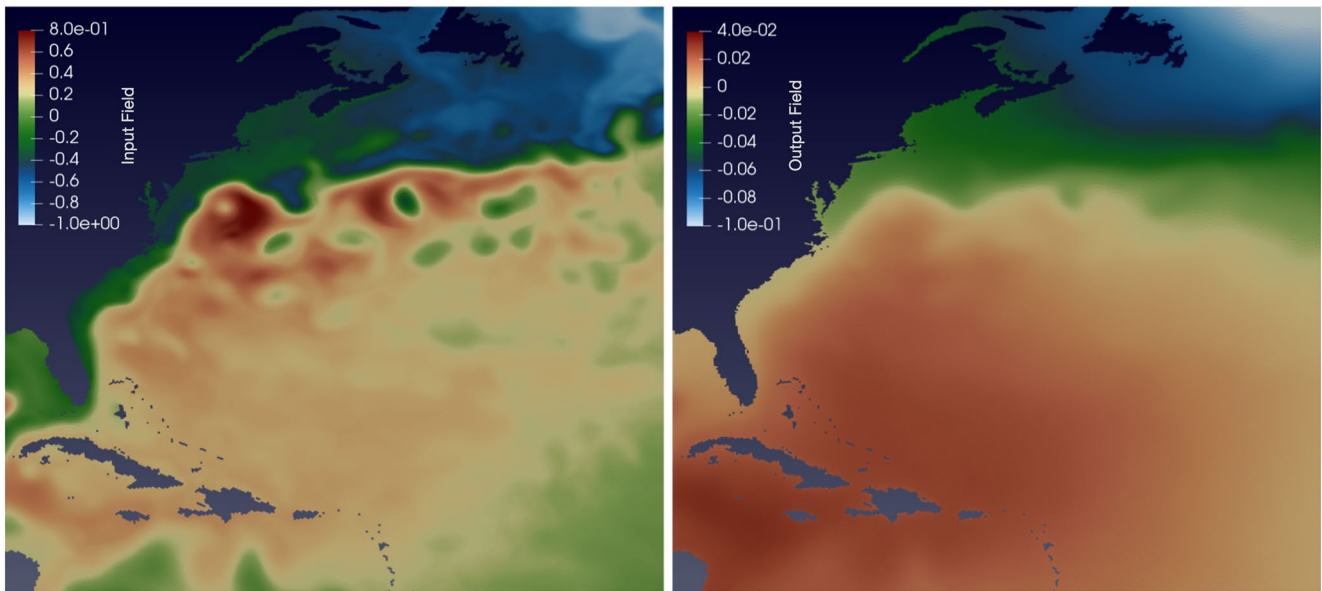
Figure 1. Example of spatially-smoothed output (right) of the self-attraction and loading (SAL) operator (Equation 6) applied to an input field (left). The SAL output has amplitude roughly 1/10 that of the original. For the barotropic runs used in this model, we evaluate SAL using the sea-surface height (SSH) signal, shown here. However, for a full baroclinic model it is necessary to use the bottom pressure as input.

Prior to our global tidal simulations, we validated the above approach by initializing the SSH to a single spherical harmonic function on the MPAS mesh, allowing us to easily confirm that the results matched the theoretical expectation.

2.3. Meshes

Several studies have demonstrated the effect of resolution on the accuracy of tidal models (Arbic et al., 2008; Egbert et al., 2004; Pringle et al., 2021). Here, we compare two types of meshes: icosahedral and variable resolution. Icosahedral meshes are spatially quasi-uniform, and have the smallest variations of cell area, vertex angles,
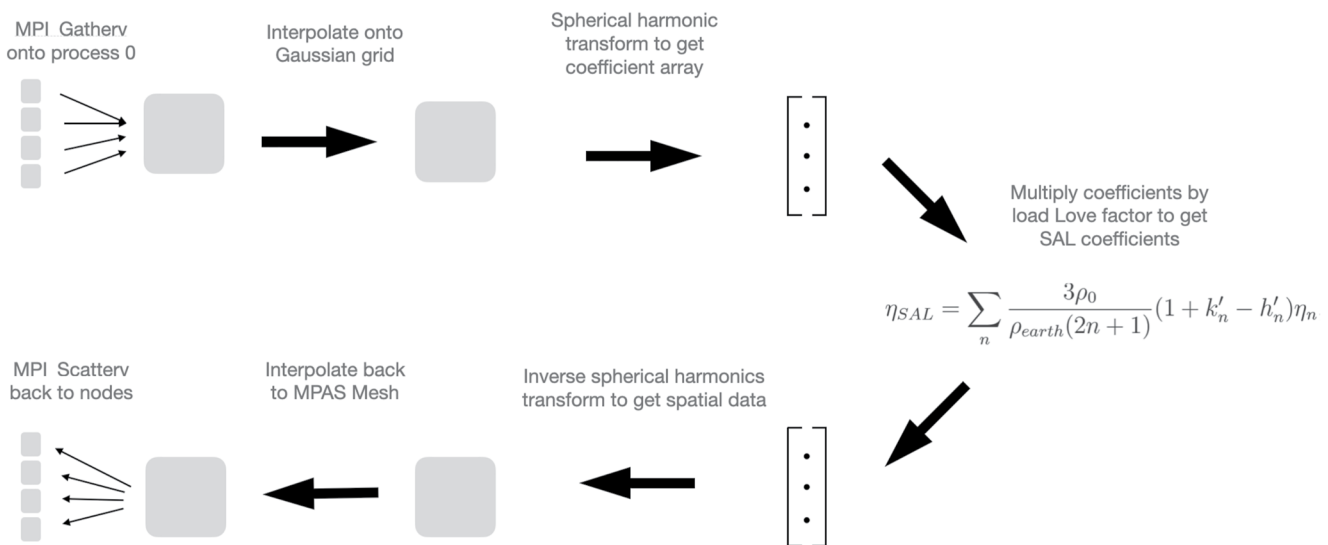
Figure 2. Overview of the procedure used to calculate self-attraction and loading (SAL). The sea-surface height (SSH) field is sent to process 0, remapped onto a Gaussian grid, then decomposed into spherical harmonics. The perturbation in SSH due to SAL is calculated and then transformed into spatial data, remapped onto the MPAS-Ocean mesh, and sent back to the nodes.

$$\eta_{SAL} = \sum_n \frac{3\rho_0}{\rho_{earth}(2n+1)}(1 + k'_n - h'_n)\eta_n$$

Table 1
Details for Each Mesh Used in the Simulations

Mesh type	Avg. cell width	Wave drag coeff.	Number of cells	Time step (s)
Icosahedron 7	62.9 km	1.80	163,842	60
Icosahedron 8	31.5 km	1.08	655,362	60
Icosahedron 9	15.7 km	0.72	2,621,442	30
Icosahedron 10	7.87 km	0.36	10,485,762	15
VR 45 to 5	45 to 5 km	0.72	2,359,578	20

Note. Cell width of a polygon is computed as the diameter of a circle with the same area.

and edge lengths across the sphere among any global meshes, so are the perfect choice for comparisons between resolutions. Table 1 shows the resolutions of the icosahedral meshes used in our simulations. The numbers 7–10 refer to the number of refinement iterations in the mesh generation process, where each iteration divides every triangle on the primal (triangular) mesh into four triangles, so that the mesh at step n contains $2 + 10 \cdot 4^n$ cells on the dual mesh (12 pentagons and the rest hexagons).

The variable resolution 45 to 5 km mesh (Figures 3 and 4) is an ADCIRC (Advanced CIRCulation)-style mesh (Pringle et al., 2021). Tides are particularly sensitive to shallow coastal areas and steep topographic gradients, where significant tidal energy dissipation takes place. In fact, about 2/3 of tidal dissipation occurs in coastal regions (Egbert & Ray, 2000, 2003). In our variable-resolution configuration, we adapt the length scale of the mesh in critical areas to better capture dynamics in shallow tidal flats and in regions of sharp bathymetric variation; employing the following mesh spacing heuristics to design a global mesh that captures local tidal processes:

$$l_{wav}(\mathbf{x}) = \beta_{wav} T_{M_2} \sqrt{g\tilde{H}}, \tag{9}$$

$$l_{slp}(\mathbf{x}) = \beta_{slp} \frac{2\pi \tilde{H}}{\nabla \tilde{H}}, \tag{10}$$

$$l^*(\mathbf{x}) = \max\left(\min\left(l_{wav}(\mathbf{x}), l_{slp}(\mathbf{x}), l_{\max}\right), l_{\min}\right), \tag{11}$$

$$l^* \rightarrow |\nabla l| \leq \gamma. \tag{12}$$

Here, $l_{wav}(\mathbf{x})$ and $l_{slp}(\mathbf{x})$ are barotropic tidal length-scale heuristics, with l_{wav} increasing mesh resolution in shallow regions to resolve the wavelength of shallow-water dynamics, and l_{slp} increasing mesh resolution in areas of large relative bathymetric gradients to capture topographically-induced flow. β_{wav} and β_{slp} are tunable "'resolution-selection" parameters, set to $\beta_{wav} = \frac{1}{80}$ and $\beta_{slp} = \frac{1}{4}$ in this study. To produce smooth distributions suitable for mesh generation, $\tilde{H}$ and $\nabla\tilde{H}$ represent Gaussian-filtered $\left(\sigma = \frac{1}{2}\right)$ depths and gradients obtained from the raw GEBCO2021 bathymetry. $l^*(\mathbf{x})$ is an initial combined estimate of mesh spacing throughout the domain, taking limiting values of l_{wav}, l_{slp} at each spatial point and clipping to $l_{\min} = 5km$ and $l_{\max} = 45km$. To control the gradation of the mesh overall, this initial estimate is "gradient-limited" to ensure the relative increase in mesh spacing is bounded below a user-defined threshold, here set to $\gamma = \frac{1}{8}$. See Figure 3 for a detailed view of the resulting mesh spacing pattern $l(\mathbf{x})$ in the North Atlantic region. Meshes in this study are generated using the `JIGSAW` unstructured meshing library (Engwirda, 2017), with pre-processing completed using the `scikit-image` package (Van der Walt et al., 2014).

2.4. Topographic Wave Drag

Tidal dissipation occurs as a stratified fluid flows over rough topography, causing energy to transfer from barotropic to baroclinic tides (Munk, 1966; Munk & Wunsch, 1998). Including this topographic wave drag has been shown to decrease the tidal elevation errors in tidal models (Arbic et al., 2004; Egbert et al., 2004; Green & Nycander, 2013; Lyard et al., 2006). Different parameterization methods exist, and several studies include comparisons of various methods (Buijsman et al., 2015; Egbert et al., 2004; Green &
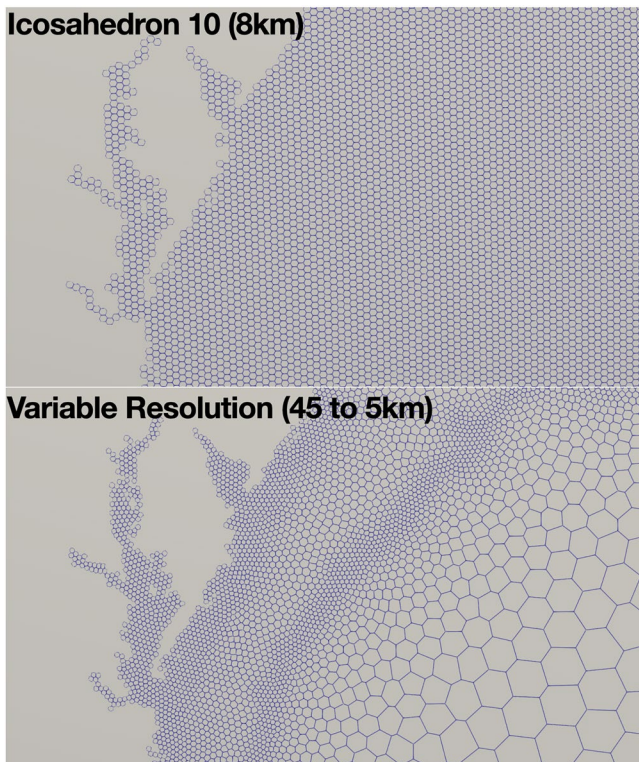
Figure 3. Comparison of the Icosahedron 10 mesh (top) and the variable resolution mesh (bottom) in the North Atlantic near Delaware Bay. The Icosahedron 10 mesh is a quasi-uniform 8-km mesh while the variable resolution mesh ranges from 45 to 5 km.
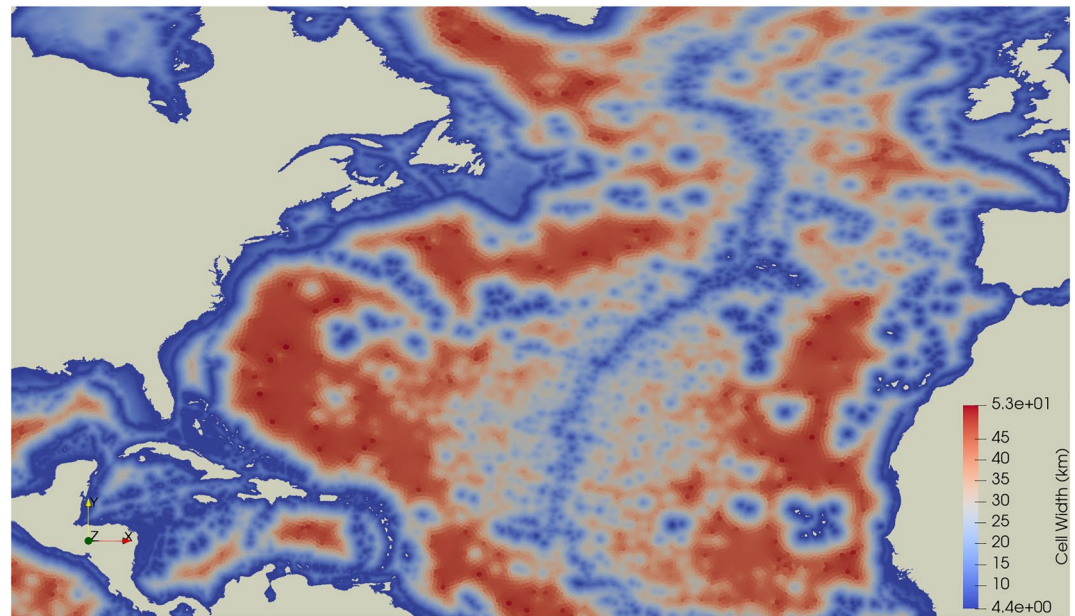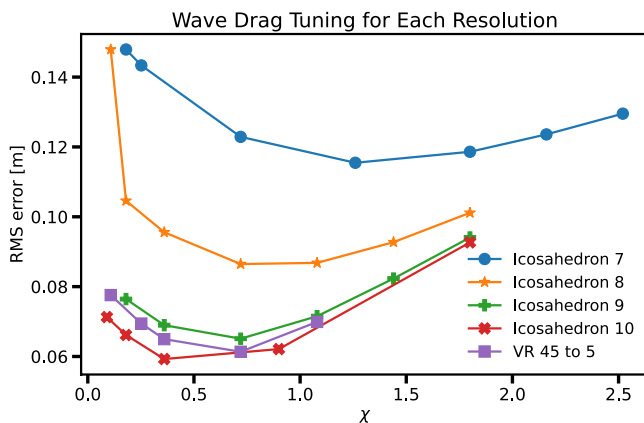
Figure 4. View of the variable resolution mesh around the Atlantic Ocean. The colors indicate the size of each cell in the mesh, with blue indicating smaller cell size and red indicating larger cell size. There is more refinement around (1) shallow depths, and (2) regions of steep topographic gradients.

Nycander, 2013). Here, we have implemented the scheme proposed by Jayne and St. Laurent (2001) which uses a simple tunable scalar,

$$C = \frac{\pi}{L} \hat{H}^2 N_b. \tag{13}$$

Here C is the same as that in Equation 1, $\hat{H}$ represents the bottom roughness and N_b is the buoyancy frequency at the bottom. L is a wave length representing the topography, which we set to 10 km, as in Jayne and St. Laurent (2001) and Buijsman et al. (2015). MPAS-Ocean reads in the Hycom variable `rinv`, which is H/C. The value of the parameter χ depends on the resolution (Arbic et al., 2008; Buijsman et al., 2020), and required a tuning of the wave drag for each mesh in this study (Figure 5).

2.5. Bathymetry

The quality of bathymetric data sets can impact the errors found in tidal models. In particular, it has been found that Hudson Bay and other areas can significantly change tides in regions around the globe (Arbic et al., 2009; Pringle et al., 2018). It was demonstrated by Arbic et al. (2009) and Arbic and Garrett (2010) that regions of large resonant coastal tides, such as Hudson Bay, have a substantial "back effect" on the global ocean tidal system. Blakely et al. (2022) showed that tidal errors can be improved by combining GEBCO bathymetry with various high-quality regional bathymetric data sets. Motivated by this, we include a comparison of two different global bathymetric data sets: GEBCO2021 (GEBCO Compilation Group, 2021) and SRTM15+ (Tozer et al., 2019), each with regional patching around Canada (Canadian Hydrographic Service, 2018), northern Australia (Beaman, 2016) and the great barrier reef (Beaman, 2020).

Figure 5. Wave drag (χ) tuning for each mesh. These were evaluated with full inline self-attraction and loading (SAL). The optimal wave drag coefficient for each mesh was used to perform all other simulations using that mesh.

Table 2
Complex M_2 *Error (cm) for All Simulations, Where Columns Show Error Calculations for Global (All Cells), Deep, and Shallow Water*

Mesh	Bathymetry	SAL type	Global	Deep	Shallow
Icosahedron 7	GEBCO2021	Inline	14.1	12.0	30.0
		Scalar	14.8	12.9	28.8
Icosahedron 8	GEBCO2021	Inline	10.7	8.8	22.5
		Scalar	12.9	11.3	22.7
Icosahedron 9	GEBCO2021	Inline	8.0	6.4	16.3
		Scalar	12.2	10.5	20.5
Icosahedron 10	GEBCO2021	Inline	7.4	5.8	14.0
		Scalar	14.3	12.2	23.8
VR 45 to 5 km	GEBCO2021	Inline	6.8	5.4	13.3
		Scalar	10.4	8.9	17.2
	SRTM15+	Inline	7.0	5.7	12.6

3. Simulation Details

3.1. Tidal Evaluation

It is common to evaluate tidal models by comparing the root-mean squared complex error (RMSE) versus a benchmark, such as TPXO8 (Egbert & Erofeeva, 2002). Here, as in Arbic et al. (2004), we separate the errors into three regions: *deep* (depths >1,000 m and between 66°N and 66°S), *shallow* (<1,000 m) and *global* (no restriction). The pointwise RMSE for the tidal constituent, which we also denote by D (for discrepancy) can be computed as:

$$D^2 = \frac{1}{2}\left(A_{TPXO}^2 + A_{MPAS}^2\right) - A_{TPXO}A_{MPAS}\cos\left(\phi_{TPXO} - \phi_{MPAS}\right), \quad (14)$$

$$RMSE_{areaweighted} = \sqrt{\frac{\iint D^2 dA}{\iint dA}}. \quad (15)$$

In Equation 15, A_{TPXO} and A_{MPAS} are the M_2 amplitudes and ϕ_{TPXO} and ϕ_{MPAS} are the phases of TPXO and MPAS-Ocean, respectively. The quantity $RMSE_{areaweighted}$ is weighted by the area dA of each cell.

We also evaluate the model against tide gauge observations as:

$$D^2 = \frac{1}{2}\left(A_{tg}^2 + A_{MPAS}^2\right) - A_{tg}A_{MPAS}\cos\left(\phi_{tg} - \phi_{MPAS}\right), \quad (16)$$

$$RMSE_{tg} = \sqrt{\sum \frac{D^2}{N_{tg}}}, \quad (17)$$

where tg denotes tide gauge data and N_{tg} is the number of tide gauge stations. For these comparisons we divide the errors into a different set of categories than we use for the TPXO comparison. These are: *deep* (depths <1,000 m), *shallow* (depths between 100 and 1,000 m), and *coastal* (depths <100 m). Note that for the tide gauge comparisons, we do not restrict latitude as we do for the TPXO comparisons.

The complete list of simulations is given in Table 2. We compare results from different Icosahedral meshes (7, 8, 9, and 10) to results from a variable resolution mesh. We also compare the results of simulations with inline SAL versus scalar SAL for the highest resolutions: Icosahedral 10 and the variable resolution. Furthermore, we tested two different bathymetric data sets: GEBCO 2021 and SRTM15+, each with and without refinement in critical areas. We ran all simulations for 120 days using a fourth-order Runge-Kutta time-stepping method. The tidal phases and amplitudes are calculated from harmonic analysis of the final 90 days of the simulation, allowing for a 30-day spin-up.

3.2. Tuning

Two parameters required tuning in order to perform these tests: a wave drag parameter and the interval at which SAL is updated.

3.2.1. Topographic Wave Drag

The MPAS-Ocean model follows the Jayne and St. Laurent drag scheme in that it has a single tunable wave drag parameter, χ, as seen in Equation 1. It is necessary to tune the wave drag parameter for each resolution to ensure optimally modeled tides and tidal energy dissipation. Table 1 shows the values chosen for each resolution with the sampled wave drag parameters for each resolution shown in Figure 5. We can also see in this figure that as χ approaches 0 (at which point wave drag would be turned off), the errors begin to increase by up to several centimeters.

Table 3
RMSE Error for M_2 *Constituent at Different SAL Update Intervals*

Calculation interval	30 min	10 min	1 min
Icosahedron 8 RMSE (cm)	8.8	8.4	8.4
Icosahedron 9 RMSE (cm)	6.4	6.4	6.5
VR 45 to 5 km RMSE (cm)	6.1	6.1	6.4

3.2.2. SAL Calculation Interval

The full inline SAL calculation can be costly, particularly at high resolution. To help reduce this computational burden, we experimented with updating the value of the SSH perturbation due to SAL at various intervals of 1, 10, and 30 min. We continue to apply SAL at every time step between the update intervals. Table 3 shows the resulting M_2 errors on the Icosahedral 8 and 9 meshes for each of these cases. Decreasing the intervals of calculation does not necessarily lead to decreased tidal errors, likely due to other sources of error dominating. Ultimately, we decided that the 30-min intervals best optimized the benefits of the inline calculation relative to the computational cost. We include further results of the computational cost in Section 4.3.

4. Results

4.1. TPXO8 Comparison

The RMSE for the M_2 tidal constituent as compared to TPXO8 are shown in Table 2. Figures 6 and 7 show the distribution of the M_2 RMS error D in the solution as compared to TPXO8. The decreasing error at finer resolutions demonstrates approximate numerical convergence. The largest errors, particularly in the variable resolution mesh, lie in the region around Antarctica. The E3SM water cycle configurations do not include ice shelf cavities. As such, we are planing a follow-up study focused on the accuracy of tides under those circumstances. For now, the simulations in this paper do not include an explicit representation of ice shelf cavities, which have been shown to impact tidal accuracy, particularly in this region (Blakely et al., 2022; Stammer et al., 2014).

Comparing the results for inline SAL and the scalar approximation (Figure 8), we can see that at every resolution, the deep (>1,000 m) RMS error improves with the inline SAL. Finer resolution meshes see a larger benefit from inclusion of inline SAL than the coarser resolutions. As the quasi-uniform meshes increase resolution, inline SAL reduces the error by as much as 50%. For the scalar SAL case, the Icosohedron 10 mesh has unusually larger errors. This could be due to keeping the β constant for all cases, rather than tuning it for specific resolutions. Additionally, the wave drag parameter χ was tuned for the inline SAL cases, so further turning may lead to more typical results for the scalar case on the Icosohedron 10 mesh. For the variable resolution mesh, the improvement is not as large but inline SAL still reduces the error by 39% as compared to the scalar SAL. The lowest error achieved is on the 45 to 5 km variable resolutions mesh, with a deep M_2 RMS error of 5.4 cm. As a point of comparison, Schindelegger et al. (2018) and Shihora et al. (2022) both included full inline SAL calculations into a barotropic tide model and found deep ocean M_2 RMS errors of 4.4 and 3.4 cm, respectively. Both studies used global 1/12° resolution regular latitude-longitude grids with ice shelf cavities included. The Schindelegger et al. (2018) model domain ranged from 86° to 84°N. M_2 RMS errors with ADCIRC were found to be 2.9 cm by Pringle et al. (2021) and were further lowered to 1.9 cm by Blakely et al. (2022). All of the previous studies used more sophisticated wave drag schemes, such as a full tensor calculation or optimization of spatially-dependent coefficients, and evaluated RMSE at depths >1,000 m and latitudes ≤ |±66°|. The two ADCIRC studies implemented SAL by reading in values from a data-assimilated model and featured a global 2 to 25-km variable resolution mesh. Stammer et al. (2014) includes a comparison of errors for various purely hydrodynamical, non-data assimilative models ranging from 5.3 to 7.8 cm. While the tidal errors in MPAS-Ocean are not as competitive as some state-of-the art models that focus exclusively on tidal modeling, they are low enough to represent tides in an Earth system model, thus paving the way for studies of tidal interactions with storm surges, rivers, or components of the cryosphere in the future (see Section 5). In at least one other run using settings not directly tested here, we have achieved an even lower RMS error of 5.1 cm, indicating there is still room for improvement.

Aside from inclusion of explicit ice-shelf cavities, the errors in our model could be improved by using a more sophisticated wave-drag scheme or a better-optimized variable resolution mesh. Optimization for improved tidal errors on the VR mesh include adjusting the maximum and minimum cell size as well as the limiting gradient that determines the relative increase in cell size. As discussed in the tuning section, the wave drag coefficient is highly dependent on the resolution of the mesh. For the variable resolution mesh, the "best" wave-drag coefficient may be different depending on the resolution of a particular region of cells. Furthermore, we may find that the scalar parameterization of wave drag is not as accurate as a full implementation. The generation of the variable mesh
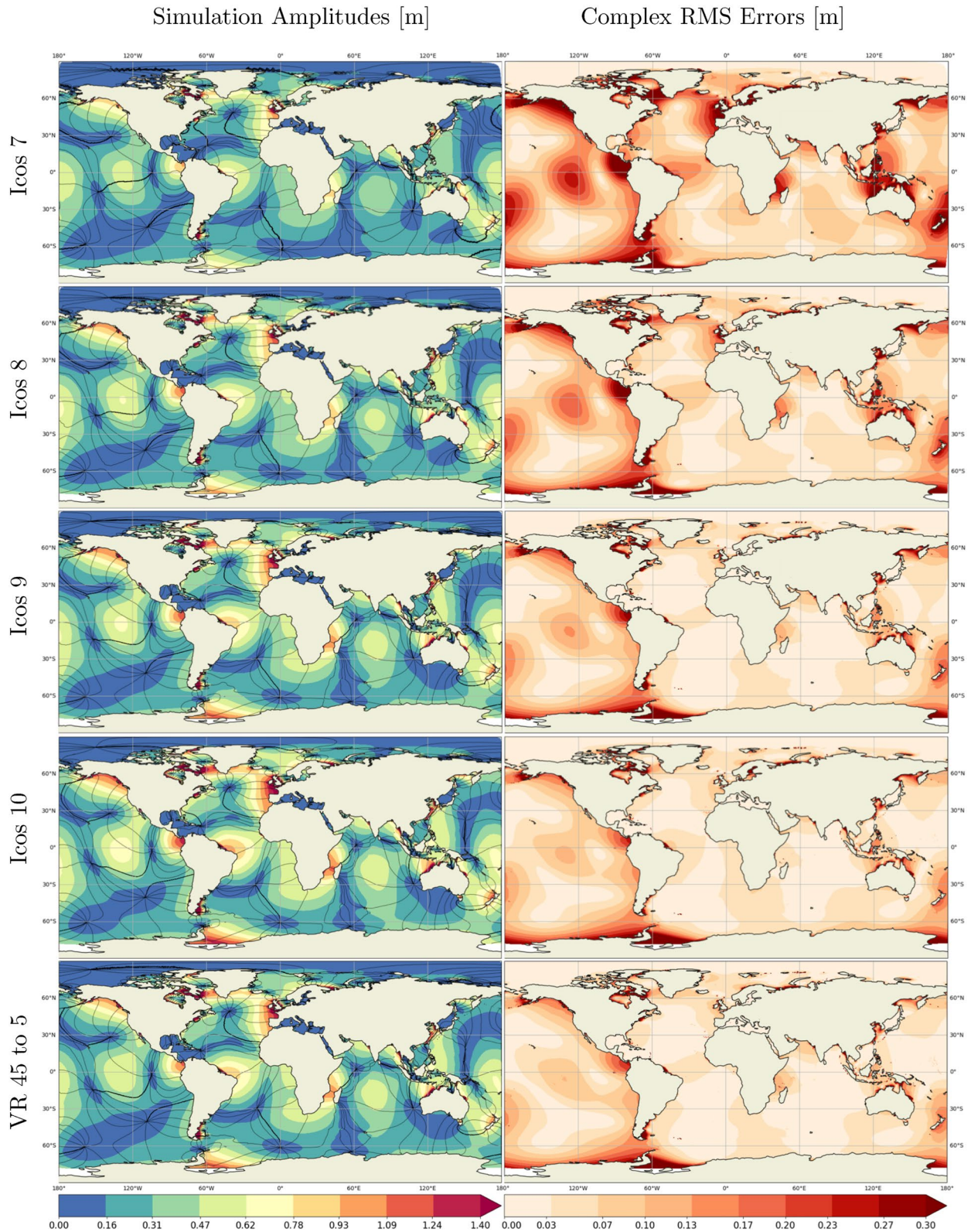
Figure 6. Pointwise complex RMS differences (D) between Model for Prediction Across Scales (MPAS) and TPXO8, showing simulated M_2 tidal amplitudes (colors) and phases (lines) from MPAS-O at various resolutions (left); M_2 RMS errors calculated with respect to TPXO8 data (right). These represent the errors on each mesh obtained from using inline self-attraction and loading (SAL) and GEBCO2021 bathymetry.
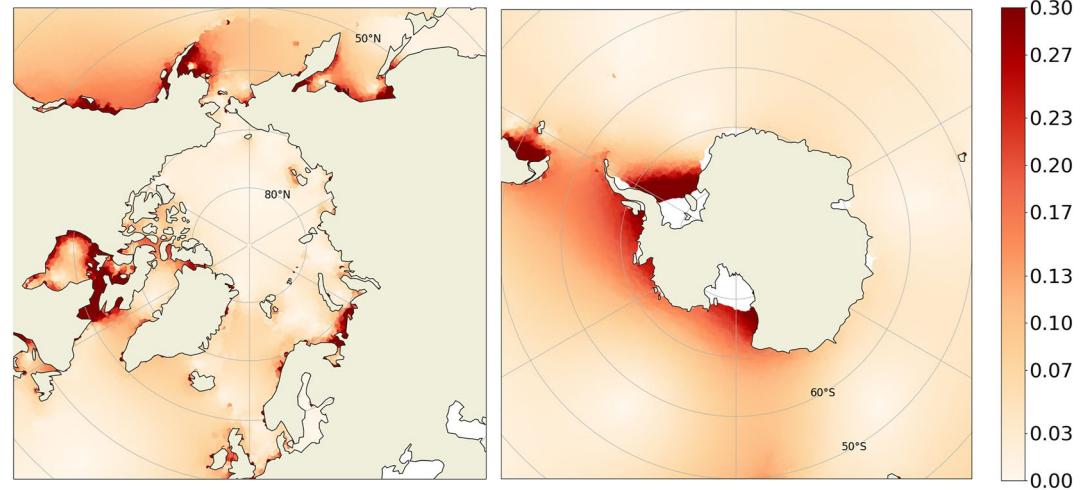
Figure 7. RMS error (m) of the variable-resolution simulation versus TPXO8 in the Arctic Ocean (left) and Southern Ocean (right).
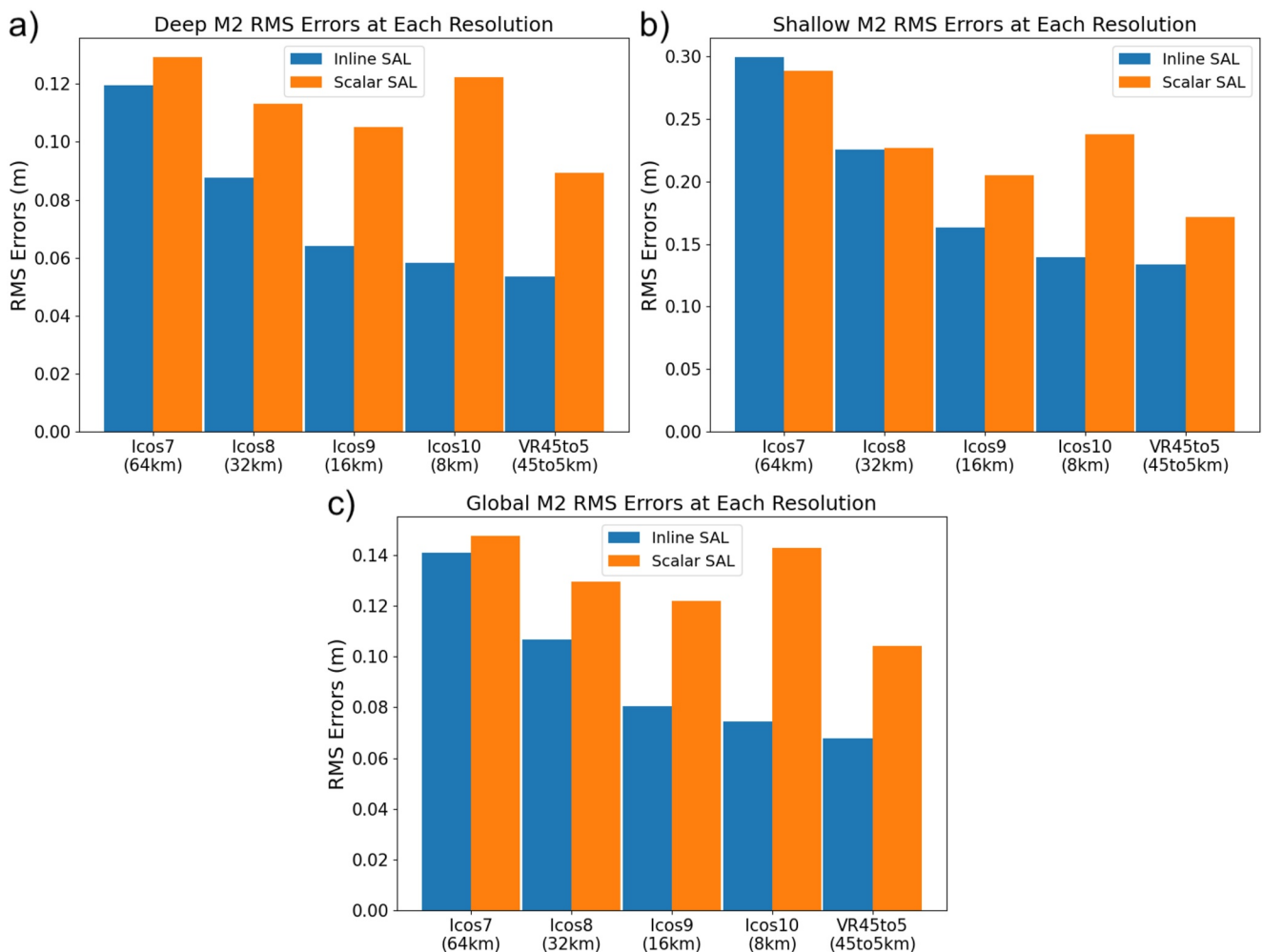
Figure 8. M_2 RMS errors relative to TPXO8 for different simulations. The plots show (a) deep regions, (b) shallow regions, and (c) global errors (see Section 3.1). Errors reduce with higher resolution, and inline self-attraction and loading (SAL) is better than scalar SAL.

itself also requires decisions about minimum/maximum cell width, and the gradient of cell width (i.e., how rapidly the cell sizes change throughout the mesh). Refining these parameters could lead to further improvement in the results found on the VR mesh.

4.2. Tide Gauge Comparison

We compare the results of MPAS-Ocean to tide gauge data sets including the "ground truth" stations (pelagic, shallow, and coastal) from Stammer et al. (2014), as well as stations from NOAA, KHOA, JMA, and GESLA. These stations were consolidated by Pringle (2019), including directly provided tidal harmonics or using UTIDE (Codiga, 2011) on time level histories. Figure 9, shows the model versus tide gauge amplitudes and phases. The tide gauge data sets have been filtered to exclude gauges generally outside of the domain of the simulation. For the phase data, we shifted the values so that the phase differences were all within 180°. The RMS error when comparing against the 151 pelagic stations is 5.8 cm for the variable resolution mesh and 5.9 cm for the 8 km quasi-uniform mesh (Table 4), which is consistent with the results seen from the TPXO8 comparison of 5.4 and 5.8 cm, respectively, for the deep ocean. For reference, in the previous studies about full inline SAL, Schindelegger et al. (2018) had an RMS error of 5.9 cm and Shihora et al. (2022) had an error of 4.8 cm when comparing to the pelagic stations.

A large majority of the tide gauges sampled are near the coasts, and we can see from the figures that MPAS-O has more accurate tides near the deep-ocean gauges (Figure 9). The R^2 value for M_2 amplitudes increases for increasing depths. In the zoomed-in plot showing only tidal amplitudes between 0 and 1 m, we can see that most of the spread is due to errors in the shallower locations (mainly regions less than 100 m deep). Comparing the two different meshes, we can see that while they both give similar results, the variable resolution mesh does outperform the quasi-uniform mesh slightly in the shallower regions. For depths less than 100m, the variable resolution mesh amplitude has a value of $R^2 = 0.950$ compared to the quasi-uniform mesh value of $R^2 = 0.933$. Similarly, for depths between 100 and 1,000 m, they have values of $R^2 = 0.974$ and $R^2 = 0.950$ respectively. For depths greater than 1,000 m, we can see a slight advantage in the quasi-uniform mesh, with a value of $R^2 = 0.986$ compared to the variable resolution mesh value of $R^2 = 0.983$. The quasi-uniform mesh has an 8 km resolution over the entire ocean, while the variable resolution mesh has cells as large as 45 km in this region. Despite the slight advantage this gives the quasi-uniform mesh for amplitudes, the variable resolution mesh also has similar or better phase results, leading to reduced RMSE (Figure 4) for this mesh. When comparing the scalar results to the inline SAL, we can see that the inline calculation performs better overall for the Icosahedron 10 mesh, but the variable resolution mesh sees most benefit in the phase errors. Even though the RMSE is higher for both meshes, the amplitude R^2 values are actually higher for the scalar while the phase values are lower. We can also consider the physical spread of errors by separating the tide gauges based on whether their errors are larger or smaller than the RMS error (Figure 10). MPAS-O tidal errors are generally greater than the total RMS error in regions near coastlines, whereas tidal errors in the deep-ocean are generally less than the RMS error. While we expect the shorelines to have larger overall tides and therefore larger errors in the model, the figure also demonstrates that many shallow regions also have lower errors. We expect that once further improvements to the variable resolution mesh allow us to resolve the coastline in better detail, these errors might reduce even further. Additionally, allowing for different wave drag coefficients for different regions may help optimize drag specifically along shelves and coastlines (e.g., Blakely et al., 2022).

4.3. Computational Scaling

We show differences between performance for the inline SAL updated at various intervals and performance on the variable resolution mesh compared to the Icosahedron mesh. All runs were performed on NERSC Cori compute nodes with 2.3 GHz Haswell processors (Intel Xeon Processor E5-2698 v3). For the mesh comparisons, the variable resolution performance is better than the Icosahedron 10 mesh (Figure 11), with comparable RMS errors (Figure 2). Table 1 shows the number of cells and the time step needed to run the model on each mesh. The variable resolution mesh allows for significantly fewer cells, leading to improved computational performance. For all meshes, the explicit time step is restricted by the advective CFL condition, defined as the ratio of the cell width to the wave propagation speed,
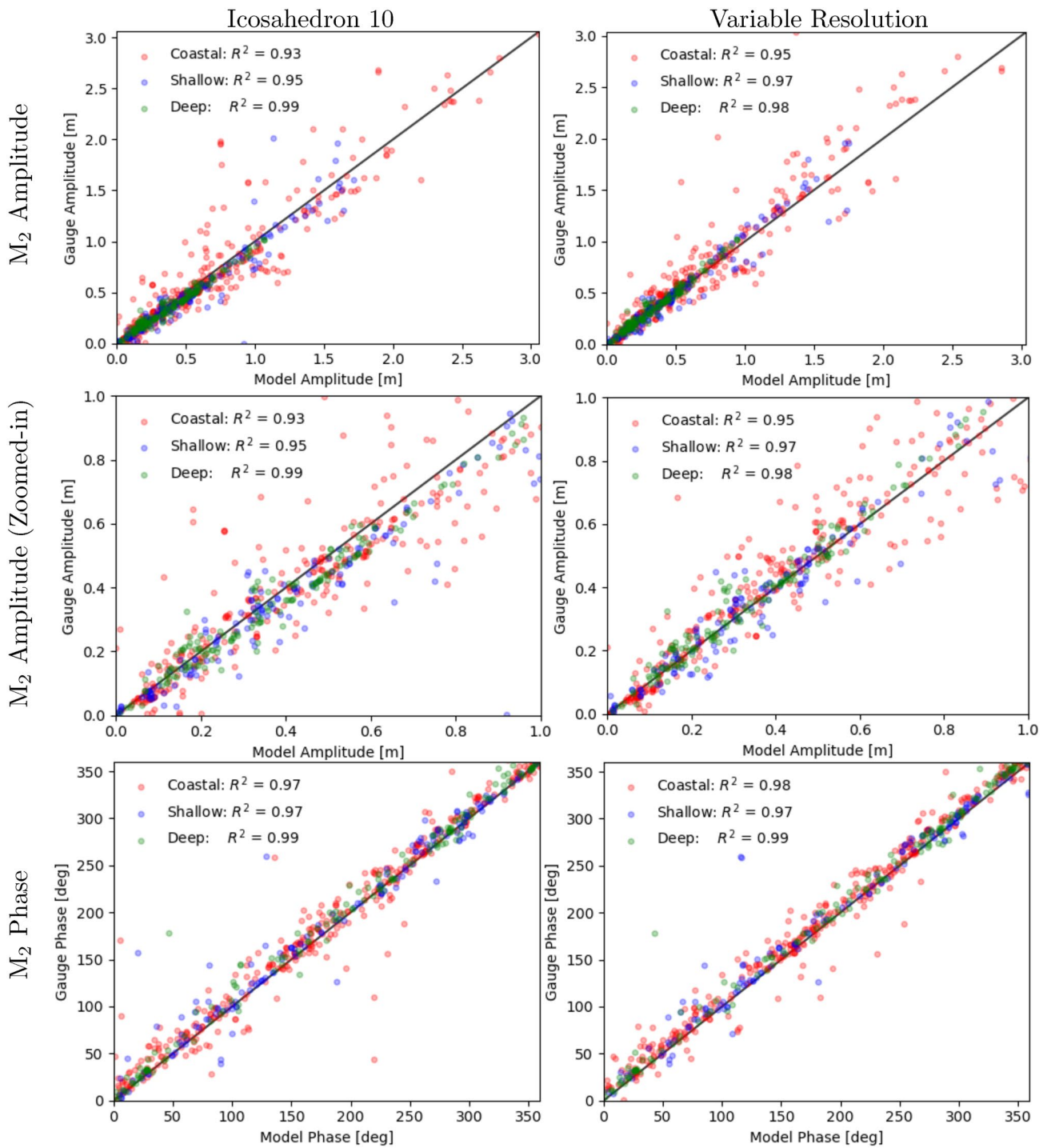
Figure 9. M_2 tidal results from inline self-attraction and loading (SAL) Icosahedron 10 run compared to tide gauge data for the deep, shallow, and coastal tide gauges (see Section 3.1). The R^2 values are given in the legend.

$$dt < \frac{\text{cell width}}{\text{wave speed}}, \quad \text{wave speed} = \sqrt{gh}, \tag{18}$$

where dt is the time step, h is the water depth, and g is the gravitational constant. In ocean flows, the surface gravity wave speed produces the fastest velocities. For the variable resolution mesh, this condition means that the

Table 4

R^2 Values for the M_2 Tide Gauge Amplitude (Top) and Phase (Bottom) Comparisons in Deep (>1,000 m), Shallow (Between 1,000 and 100 m, and Coastal (<100 m) Regions

Mesh	SAL type	RMSE (pelagic)		Deep	R^2 Shallow	Coastal
Icosahedron 10	Inline	5.9	Amplitude	0.986	0.950	0.933
	Scalar	13.1		0.982	0.952	0.928
VR 45 to 5 km	Inline	5.8		0.983	0.974	0.950
	Scalar	9.3		0.986	0.982	0.959
Icosahedron 10	Inline		Phase	0.993	0.975	0.974
	Scalar			0.991	0.933	0.965
VR 45 to 5 km	Inline			0.994	0.969	0.985
	Scalar			0.993	0.930	0.979

Note. The complex RMS error (cm) for the 151 "Ground Truth" pelagic stations is also included.
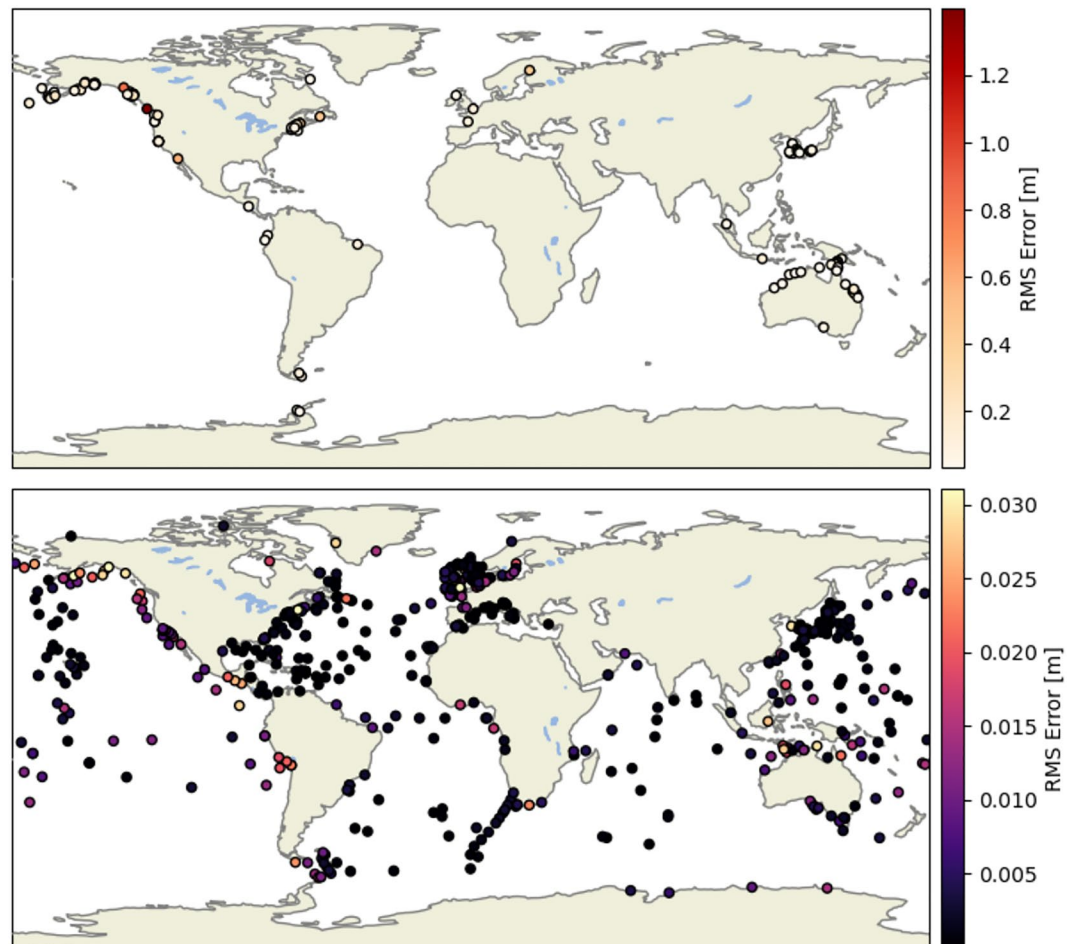
Figure 10. Global distribution of tide gauges, colored by model error from the variable resolution mesh simulation. The top plot shows locations with errors greater than the RMS value of all stations, and the bottom plot shows gauges with errors less than the RMS value. The majority of points have a small error, while the small number of stations with large error are near coastlines. This analysis is restricted to gauges at depths ≥100 m.
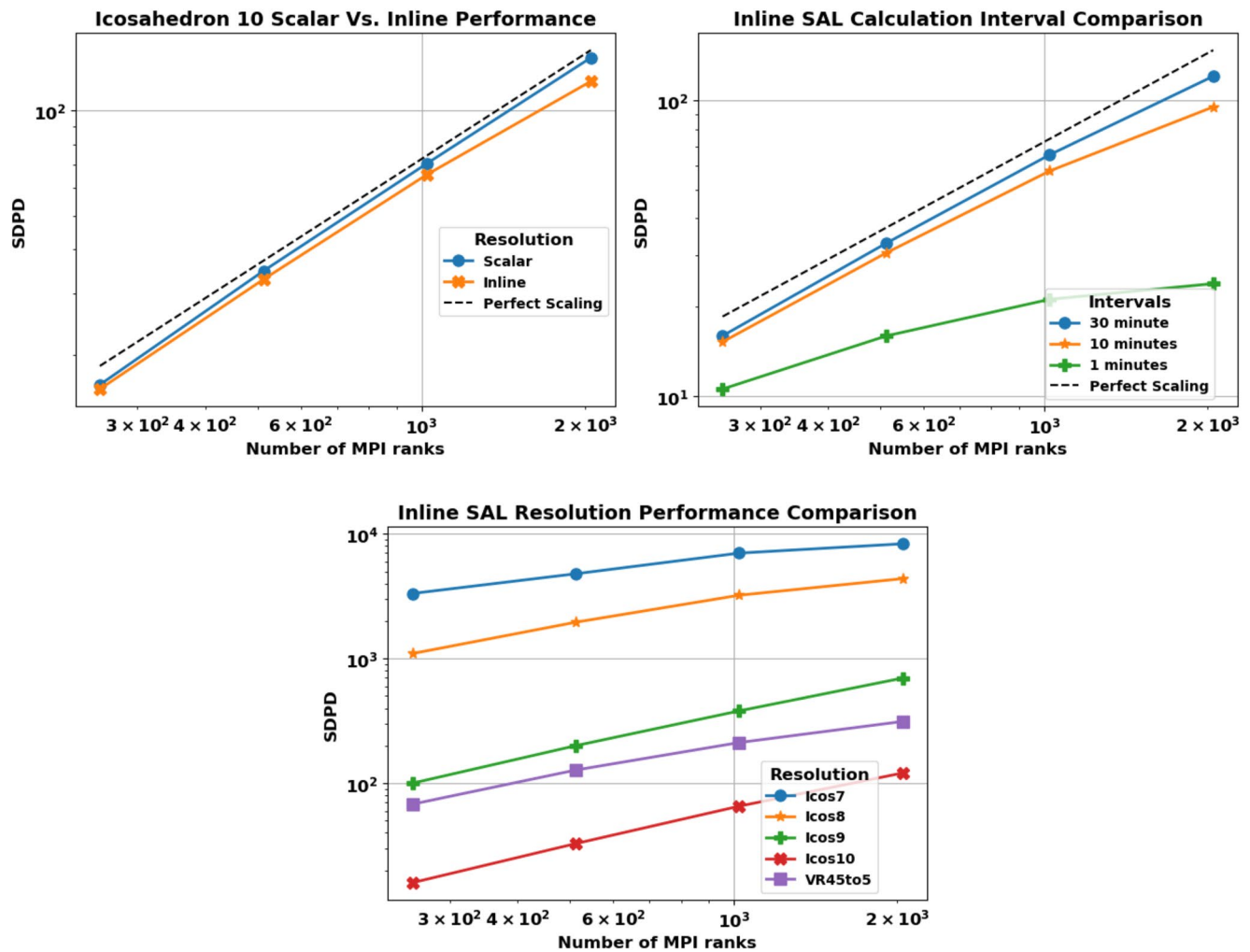
Figure 11. Performance comparisons of Model for Prediction Across Scales (MPAS-Ocean) including: scalar versus inline on Icosahedron 10; self-attraction and loading (SAL) update intervals at 1, 10, and 30 min; and performance with inline SAL on all of the meshes used in this study. The computational throughput is measured in units of simulated days per day (SDPD).

time step is not necessarily limited by the minimum cell size alone, but by the relationship between cell sizes and wave speeds throughout the domain. Noting that our variable resolution heuristics (see Section 2.3) place fine resolution in shallower, and hence lower wave-speed regions, the overall CFL restriction is found to be significantly less onerous than quasi-uniform configurations that employ higher resolution in the deep ocean. In our simulations, not only does the 45 to 5 km mesh have fewer cells than the 8 km mesh and higher resolution around the coasts, it also runs with a larger time step as can be seen in Table 1.

While the inline SAL calculations do increase the computational cost, Table 3 shows that there is only a small difference in the RMS error when updating the SAL term at larger intervals than the model time step. In fact, at higher resolutions we see that the more frequent updates may lead to higher errors. Figure 11, which plots simulation run time performance, demonstrates that updating the SAL perturbation every 30 min can improve the computational performance as compared to evaluation at more frequent time steps. When using a 30 min interval, the computational performance of the full SAL calculation is only marginally larger than the scalar implementation. Based on the scaling and the RMS errors, either 30 min or 10 min may actually be the ideal update interval for the SAL, providing computational benefit over the 1 min or more frequent intervals with little decrease in tidal accuracy.

5. Conclusions

In this paper, we demonstrated the feasibility of calculating tides within the MPAS-Ocean model employing a full inline SAL calculation in high-resolution barotropic simulations. We also examined sensitivities of the modeled tide to the SAL calculation method, careful selection of bathymetric data sets, model resolution, and a tuned wave drag coefficient. The full SAL calculations showed decreases in tidal RMS elevation errors of several centimeters across all meshes tested, relative to results computed using the scalar approximation for SAL. The variable resolution mesh had tidal errors similar to that of the Icosahedron 10 mesh, but with better computational performance, lying closer to results computed on the Icosahedron 9 mesh. Comparison of simulations using the different bathymetric data sets show that GEBCO2021 slightly outperforms SRTM15+ on the variable resolution mesh. The computational performance of the full SAL can incur large costs when evaluated at every time step. It appears that this cost can be mitigated by updating SAL at 10 or 30 min intervals, rather than at every time step, with little effect on tidal errors. Another avenue for increasing the computational efficiency is evaluation of the spherical harmonics in parallel, rather than the serial routines implemented by the SHTns package used in this study. This can be done by evaluating the integrals directly on the MPAS mesh so that the interpolation step is not needed, as pursued in a related study by our group. Comparison to tide gauge data shows that this first attempt at including tides results in slightly larger errors than tides in some other models (e.g., Blakely et al., 2022; Pringle et al., 2021; Schindelegger et al., 2018; Stammer et al., 2014). However, we expect that the RMS errors for the M_2 tide could be improved with (a) variable resolution meshes with smaller minimum cell size, (b) optimization of parameters in the variable resolution mesh generation, (c) the addition of a spatially-dependent wave drag coefficient or a more sophisticated wave drag scheme (e.g., Green & Nycander, 2013), and (d) the inclusion of ice-shelf cavities.

It is becoming clear that inclusion of tides is important for predictions of future climate and extreme sea level events (Bindoff et al., 2019; Oppenheimer et al., 2019). Our results show that MPAS-Ocean has relatively low tidal errors that are small enough to merit inclusion within a full climate system model. An important difference between the setup described for the barotropic case in this paper, and the setup needed for use in a full baroclinic framework, is the variable which is used in the SAL calculations. As mentioned in the discussion on SAL, tidal elevations can be used for spherical harmonic decomposition in the barotropic case because it is a direct measure of the mass of the water column. By contrast, baroclinic simulations require bottom pressure anomalies for this purpose. Furthermore, implementation of tides in a baroclinic model calls for some modifications to the topographic wave drag, such as by applying wave drag to the flow averaged over the bottom 500 m (e.g., Arbic et al., 2018) or using different parameter optimizations. The addition of tides in an Earth system model will allow us to examine a number of advanced aspects in the physical Earth system. For example, there is a need for inclusion of tides when considering the Arctic ocean and sea ice (Holloway & Proshutinsky, 2007) as tides can have a substantial effect on sea ice volume and salinity (Luneva et al., 2015). A review of tidal influences on ice sheets by Padman et al. (2018) suggests that feedback between ice shelf geometry and tidal currents could imply a need for explicit tides in Earth system models; see also Williams et al. (1985), Dinniman et al. (2016). Tides also have important effects on estuaries. Ruault et al. (2020) found that baroclinic tides can influence the Amazon plume, which itself can impact the Atlantic climate (Jahfer et al., 2017). High-frequency interactions of tides with storm surges and fluvial processes in estuaries (Orton et al., 2012; Spicer et al., 2019) are important for predicting coastal flooding during extreme weather events. In future studies, we plan to use MPAS-Ocean to explore these interactions between tides and other components of the Earth system (e.g., ice shelves and basal melt rates, sea ice, estuaries) and their potential impacts on future climate.

Data Availability Statement

Software for this research is available at Barton et al. (2022b) (https://doi.org/10.5281/zenodo.7025138). The initial files needed to run the model with the same configuration are available from Barton et al. (2022a) (https://doi.org/10.5281/zenodo.7019897). Model output data sets, analysis scripts, and instructions needed to reproduce the figures and tables in this paper may be found at Barton et al. (2022c) (https://doi.org/10.5281/zenodo.7019903).

References

Accad, Y., & Pekeris, C. L. (1978). Solution of the tidal equations for the M2 and S2 tides in the world oceans from a knowledge of the tidal potential alone. *Philosophical Transactions of the Royal Society of London Series A: Mathematical and Physical Sciences*, *290*(1368), 235–266. https://doi.org/10.1098/rsta.1978.0083

Arbic, B. K., Alford, M. H., Ansong, J. K., Buijsman, M. C., Ciotti, R. B., Farrar, J. T., et al. (2018). A primer on global internal tide and internal gravity wave continuum modeling in HYCOM and MITgcm. *New Frontiers in Operational Oceanography*. https://doi.org/10.17125/gov2018.ch13

Arbic, B. K., Garner, S. T., Hallberg, R. W., & Simmons, H. L. (2004). The accuracy of surface elevations in forward global barotropic and baroclinic tide models. *Deep Sea Research Part II: Topical Studies in Oceanography*, *51*(25–26), 3069–3101. https://doi.org/10.1016/j.dsr2.2004.09.014

Arbic, B. K., & Garrett, C. (2010). A coupled oscillator model of shelf and ocean tides. *Continental Shelf Research*, *30*(6), 564–574. https://doi.org/10.1016/j.csr.2009.07.008

Arbic, B. K., Karsten, R. H., & Garrett, C. (2009). On tidal resonance in the global ocean and the back-effect of coastal tides upon open-ocean tides. *Atmosphere-Ocean*, *47*(4), 239–266. https://doi.org/10.3137/oc311.2009

Arbic, B. K., Mitrovica, J. X., MacAyeal, D. R., & Milne, G. A. (2008). On the factors behind large Labrador Sea tides during the last glacial cycle and the potential implications for Heinrich events. *Paleoceanography*, *23*(3), 001573. https://doi.org/10.1029/2007pa001573

Arbic, B. K., Wallcraft, A. J., & Metzger, E. J. (2010). Concurrent simulation of the eddying general circulation and tides in a global ocean model. *Ocean Modelling*, *32*(3–4), 175–187. https://doi.org/10.1016/j.ocemod.2010.01.007

Barton, K., Pal, N., Brus, S., Petersen, M., & Engwirda, D. (2022a). MPAS-Ocean Barotropic Tidal Simulation Run Directories [Dataset]. Zenodo. https://doi.org/10.5281/zenodo.7019897

Barton, K., Pal, N., Brus, S., Petersen, M., & Engwirda, D. (2022b). knbarton/E3SM: Barotropic tides and inline SAL study Archive [Software]. Zenodo. https://doi.org/10.5281/zenodo.7025138

Barton, K., Pal, N., Brus, S., Petersen, M., & Engwirda, D. (2022c). MPAS-Ocean Barotropic Tidal Simulation Analysis [Dataset]. Zenodo. https://doi.org/10.5281/zenodo.7019903

Beaman, R. (2016). High-resolution depth model for the Northern Australia—100 m. Retrieved from https://www.deepreef.org/2017/02/28/nthaus-bathy/

Beaman, R. (2020). High-resolution depth model for the Great Barrier Reef and Coral Sea-100m [Dataset]. Geoscience Australia, Canberra. http://dx.doi.org/10.26186/5e2f8bb629d07

Bindoff, N. L., Cheung, W. W., Kairo, J. G., Arístegui, J., Guinder, V. A., Hallberg, R., et al. (2019). Changing ocean, marine ecosystems, and dependent communities. In *IPCC special report on the ocean and cryosphere in a changing climate*, (pp. 477–587). https://doi.org/10.1017/9781009157964.007

Blakely, C. P., Ling, G., Pringle, W. J., Contreras, M. T., Wirasaet, D., Westerink, J. J., et al. (2022). Dissipation and Bathymetric sensitivities in an unstructured mesh global tidal model. *Journal of Geophysical Research: Oceans*, *127*(5), e2021JC018178. https://doi.org/10.1029/2021jc018178

Bryan, K. (1969). A numerical method for the study of the circulation of the world ocean. *Journal of Computational Physics*, *4*(3), 347–376. https://doi.org/10.1016/0021-9991(69)90004-7

Buijsman, M. C., Ansong, J. K., Arbic, B. K., Richman, J. G., Shriver, J. F., Timko, P. G., et al. (2016). Impact of parameterized internal wave drag on the semidiurnal energy balance in a global ocean circulation model. *Journal of Physical Oceanography*, *46*(5), 1399–1419. https://doi.org/10.1175/jpo-d-15-0074.1

Buijsman, M. C., Arbic, B. K., Green, J., Helber, R. W., Richman, J. G., Shriver, J. F., et al. (2015). Optimizing internal wave drag in a forward barotropic model with semidiurnal tides. *Ocean Modelling*, *85*, 42–55. https://doi.org/10.1016/j.ocemod.2014.11.003

Buijsman, M. C., Stephenson, G. R., Ansong, J. K., Arbic, B. K., Green, J. M., Richman, J. G., et al. (2020). On the interplay between horizontal resolution and wave drag and their effect on tidal baroclinic mode waves in realistic global ocean simulations. *Ocean Modelling*, *152*, 101656. https://doi.org/10.1016/j.ocemod.2020.101656

Canadian Hydrographic Service. (2018). Canadian hydrographic Service non-navigational (NONNA) Bathymetric data [Dataset]. stl. Retrieved from https://open.canada.ca/data/en/dataset/d3881c4c-650d-4070-bf9b-1e00aabf0a1d

Codiga, D. L. (2011). *Unified tidal analysis and prediction using the utide matlab functions (Technical Report)*. Graduate School of Oceanography, University of Rhode Island. https://doi.org/10.13140/RG.2.1.3761.2008

Cummins, P. F., & Oey, L.-Y. (1997). Simulation of barotropic and baroclinic tides off northern British Columbia. *Journal of Physical Oceanography*, *27*(5), 762–781. https://doi.org/10.1175/1520-0485(1997)027<0762:sobabt>2.0.co;2

Dinniman, M. S., Asay-Davis, X. S., Galton-Fenzi, B. K., Holland, P. R., Jenkins, A., & Timmermann, R. (2016). Modeling ice shelf/ocean interaction in Antarctica: A review. *Oceanography*, *29*(4), 144–153. https://doi.org/10.5670/oceanog.2016.106

Dushaw, B. D., Egbert, G. D., Worcester, P. F., Cornuelle, B. D., Howe, B. M., & Metzger, K. (1997). A TOPEX/POSEIDON global tidal model (TPXO.2) and barotropic tidal currents determined from long-range acoustic transmissions. *Progress in Oceanography*, *40*(1–4), 337–367. https://doi.org/10.1016/s0079-6611(98)00008-1

Egbert, G. D., & Erofeeva, S. Y. (2002). Efficient inverse modeling of barotropic ocean tides. *Journal of Atmospheric and Oceanic Technology*, *19*(2), 183–204. https://doi.org/10.1175/1520-0426(2002)019<0183:eimobo>2.0.co;2

Egbert, G. D., & Ray, R. D. (2000). Significant dissipation of tidal energy in the deep ocean inferred from satellite altimeter data. *Nature*, *405*(6788), 775–778. https://doi.org/10.1038/35015531

Egbert, G. D., & Ray, R. D. (2003). Semi-diurnal and diurnal tidal dissipation from TOPEX/Poseidon altimetry. *Geophysical Research Letters*, *30*(17). https://doi.org/10.1029/2003gl017676

Egbert, G. D., Ray, R. D., & Bills, B. G. (2004). Numerical modeling of the global semidiurnal tide in the present day and in the last glacial maximum. *Journal of Geophysical Research*, *109*(C3), jc001973. https://doi.org/10.1029/2003jc001973

Engwirda, D. (2017). JIGSAW-GEO (1.0): Locally orthogonal staggered unstructured grid generation for general circulation modelling on the sphere. *Geoscientific Model Development*, *10*(6), 2117–2140. https://doi.org/10.5194/gmd-10-2117-2017

Flick, R. E., Murray, J. F., & Ewing, L. C. (2003). Trends in United States tidal datum statistics and tide range. *Journal of Waterway, Port, Coastal, and Ocean Engineering*, *129*(4), 155–164. https://doi.org/10.1061/(asce)0733-950x(2003)129:4(155)

GEBCO Compilation Group. (2021). GEBCO 2021 grid. https://doi.org/10.5285/c6612cbe-50b3-0cff-e053-6c86abc09f8f

Golaz, J.-C., Caldwell, P. M., Van Roekel, L. P., Petersen, M. R., Tang, Q., Wolfe, J. D., et al. (2019). The DOE E3SM coupled model version 1: Overview and evaluation at standard resolution. *Journal of Advances in Modeling Earth Systems*, *11*(7), 2089–2129. https://doi.org/10.1029/2018MS001603

Gordeev, R., Kagan, B., & Polyakov, E. (1977). The effects of loading and self-attraction on global ocean tides: The model and the results of a numerical experiment. *Journal of Physical Oceanography*, *7*(2), 161–170. https://doi.org/10.1175/1520-0485(1977)007<0161:teolas>2.0.co;2

Green, J. M., & Nycander, J. (2013). A comparison of tidal conversion parameterizations for tidal models. *Journal of Physical Oceanography*, *43*(1), 104–119. https://doi.org/10.1175/jpo-d-12-023.1

Griffies, S. M., Böning, C., Bryan, F. O., Chassignet, E. P., Gerdes, R., Hasumi, H., et al. (2000). Developments in ocean climate modelling. *Ocean Modelling*, *2*(3–4), 123–192. https://doi.org/10.1016/s1463-5003(00)00014-7

Haigh, I. D., Pickering, M. D., Green, J. M., Arbic, B. K., Arns, A., Dangendorf, S., et al. (2020). The tides they are a-Changin': A comprehensive review of past and future nonastronomical changes in tides, their driving mechanisms, and future implications. *Reviews of Geophysics*, *58*(1), e2018RG000636. https://doi.org/10.1029/2018rg000636

Hendershott, M. (1972). The effects of solid Earth deformation on global ocean tides. *Geophysical Journal International*, *29*(4), 389–402. https://doi.org/10.1111/j.1365-246x.1972.tb06167.x

Holloway, G., & Proshutinsky, A. (2007). Role of tides in Arctic ocean/ice climate. *Journal of Geophysical Research*, *112*(C4), C04S06. https://doi.org/10.1029/2006jc003643

Jahfer, S., Vinayachandran, P., & Nanjundiah, R. S. (2017). Long-term impact of Amazon river runoff on northern hemispheric climate. *Scientific Reports*, *7*(1), 1–9. https://doi.org/10.1038/s41598-017-10750-y

Jay, D. A. (2009). Evolution of tidal amplitudes in the eastern Pacific Ocean. *Geophysical Research Letters*, *36*(4), L04603. https://doi.org/10.1029/2008gl036185

Jayne, S. R., & St. Laurent, L. C. (2001). Parameterizing tidal dissipation over rough topography. *Geophysical Research Letters*, *28*(5), 811–814. https://doi.org/10.1029/2000gl012044

Kang, S., Foreman, M., Crawford, W., & Cherniawsky, J. (2000). Numerical modeling of internal tide generation along the Hawaiian Ridge. *Journal of Physical Oceanography*, *30*(5), 1083–1098. https://doi.org/10.1175/1520-0485(2000)030<1083:nmoitg>2.0.co;2

Le Provost, C., Genco, M., Lyard, F. H., Vincent, P., & Canceil, P. (1994). Spectroscopy of the world ocean tides from a finite element hydrodynamic model. *Journal of Geophysical Research*, *99*(C12), 24777–24797. https://doi.org/10.1029/94jc01381

Luneva, M. V., Aksenov, Y., Harle, J. D., & Holt, J. T. (2015). The effects of tides on the water mass mixing and sea ice in the Arctic Ocean. *Journal of Geophysical Research: Oceans*, *120*(10), 6669–6699. https://doi.org/10.1002/2014jc010310

Lyard, F. H., Allain, D. J., Cancet, M., Carrère, L., & Picot, N. (2021). FES2014 global ocean tide atlas: Design and performance. *Ocean Science*, *17*(3), 615–649. https://doi.org/10.5194/os-17-615-2021

Lyard, F. H., Lefevre, F., Letellier, T., & Francis, O. (2006). Modelling the global ocean tides: Modern insights from FES2004. *Ocean Dynamics*, *56*(5), 394–415. https://doi.org/10.1007/s10236-006-0086-x

Merrifield, M. A., Holloway, P. E., & Johnston, T. S. (2001). The generation of internal tides at the Hawaiian Ridge. *Geophysical Research Letters*, *28*(4), 559–562. https://doi.org/10.1029/2000gl011749

Müller, M., Arbic, B. K., & Mitrovica, J. (2011). Secular trends in ocean tides: Observations and model results. *Journal of Geophysical Research*, *116*(C5), C05013. https://doi.org/10.1029/2010jc006387

Müller, M., Cherniawsky, J., Foreman, M., & von Storch, J.-S. (2012). Global M2 internal tide and its seasonal variability from high resolution ocean circulation and tide modeling. *Geophysical Research Letters*, *39*(19), gl053320. https://doi.org/10.1029/2012gl053320

Munk, W. H. (1966). Abyssal recipes. *Deep Sea Research and Oceanographic Abstracts*, *13*(4), 707–730. https://doi.org/10.1016/0011-7471(66)90602-4

Munk, W. H., & Wunsch, C. (1998). Abyssal recipes II: Energetics of tidal and wind mixing. *Deep Sea Research Part I: Oceanographic Research Papers*, *45*(12), 1977–2010. https://doi.org/10.1016/s0967-0637(98)00070-3

Oppenheimer, M., Glavovic, B., Hinkel, J., van de Wal, R., Magnan, A. K., Abd-Elgawad, A., et al. (2019). Sea level rise and implications for low lying islands, coasts and communities. In *IPCC special report on the ocean and cryosphere in a changing climate*. https://doi.org/10.1017/9781009157964.006

Orton, P., Georgas, N., Blumberg, A., & Pullen, J. (2012). Detailed modeling of recent severe storm tides in estuaries of the New York City region. *Journal of Geophysical Research*, *117*(C9). https://doi.org/10.1029/2012jc008220

Padman, L., Siegfried, M. R., & Fricker, H. A. (2018). Ocean tide influences on the Antarctic and Greenland ice sheets. *Reviews of Geophysics*, *56*(1), 142–184. https://doi.org/10.1002/2016rg000546

Parke, M. E., & Hendershott, M. C. (1980). M2, S2, K1 models of the global ocean tide on an elastic Earth. *Marine Geodesy*, *3*(1–4), 379–408. https://doi.org/10.1080/01490418009388005

Pekeris, C. L., & Accad, Y. (1969). Solution of Laplace's equations for the M2 tide in the world oceans. *Philosophical Transactions of the Royal Society of London—Series A: Mathematical and Physical Sciences*, *265*(1165), 413–436. https://doi.org/10.1098/rsta.1969.0062

Petersen, M. R., Asay-Davis, X. S., Berres, A. S., Chen, Q., Feige, N., Hoffman, M. J., et al. (2019). An evaluation of the ocean and sea ice climate of E3SM using MPAS and interannual CORE-II forcing. *Journal of Advances in Modeling Earth Systems*, *11*(5), 1438–1458. https://doi.org/10.1029/2018ms001373

Pringle, W. J. (2019). Global tide gauge database [Dataset]. stl Retrieved from https://www.google.com/maps/d/u/0/viewer?mid=1yvnYoLUFS9kcB5LnJEdyxk2qz6g

Pringle, W. J., Wirasaet, D., Roberts, K. J., & Westerink, J. J. (2021). Global storm tide modeling with adcirc v55: Unstructured mesh design and performance. *Geoscientific Model Development*, *14*(2), 1125–1145. https://doi.org/10.5194/gmd-14-1125-2021

Pringle, W. J., Wirasaet, D., Suhardjo, A., Meixner, J., Westerink, J. J., Kennedy, A. B., & Nong, S. (2018). Finite-element barotropic model for the Indian and Western Pacific Oceans: Tidal model-data comparisons and sensitivities. *Ocean Modelling*, *129*, 13–38. https://doi.org/10.1016/j.ocemod.2018.07.003

Ray, R. D. (1993). Global ocean tide models on the eve of TOPEX/POSEIDON. *IEEE Transactions on Geoscience and Remote Sensing*, *31*(2), 355–364. https://doi.org/10.1109/36.214911

Ray, R. D. (1998). Ocean self-attraction and loading in numerical tidal models. *Marine Geodesy*, *21*(3), 181–192. https://doi.org/10.1080/01490419809388134

Ray, R. D. (2006). Secular changes of the M2 tide in the Gulf of Maine. *Continental Shelf Research*, *26*(3), 422–427. https://doi.org/10.1016/j.csr.2005.12.005

Ringler, T., Petersen, M., Higdon, R. L., Jacobsen, D., Jones, P. W., & Maltrud, M. (2013). A multi-resolution approach to global ocean modeling. *Ocean Modelling*, *69*, 211–232. https://doi.org/10.1016/j.ocemod.2013.04.010

Rocha, C. B., Chereskin, T. K., Gille, S. T., & Menemenlis, D. (2016). Mesoscale to submesoscale wavenumber spectra in Drake Passage. *Journal of Physical Oceanography*, *46*(2), 601–620. https://doi.org/10.1175/jpo-d-15-0087.1

Ruault, V., Jouanno, J., Durand, F., Chanut, J., & Benshila, R. (2020). Role of the tide on the structure of the Amazon plume: A numerical modeling approach. *Journal of Geophysical Research: Oceans*, *125*(2), e2019JC015495. https://doi.org/10.1029/2019jc015495

Schaeffer, N. (2013). Efficient spherical harmonic transforms aimed at pseudospectral numerical simulations. *Geochemistry, Geophysics, Geosystems*, *14*(3), 751–758. https://doi.org/10.1002/ggge.20071

Schindelegger, M., Green, J., Wilmes, S.-B., & Haigh, I. D. (2018). Can we model the effect of observed sea level rise on tides? *Journal of Geophysical Research: Oceans*, *123*(7), 4593–4609. https://doi.org/10.1029/2018jc013959

Schwiderski, E. W. (1979). *Global Ocean tides. Part II. The semidiurnal principal lunar tide (M2), atlas of tidal charts and maps (Technical Report)*. Naval Surface Weapons Center. Retrieved from https://apps.dtic.mil/sti/citations/ADA084694

Shihora, L., Sulzbach, R., Dobslaw, H., & Thomas, M. (2022). Self-attraction and loading feedback on ocean dynamics in both shallow water equations and primitive equations. *Ocean Modelling*, *169*, 101914. https://doi.org/10.1016/j.ocemod.2021.101914

Shum, C., Woodworth, P., Andersen, O., Egbert, G. D., Francis, O., King, C., et al. (1997). Accuracy assessment of recent ocean tide models. *Journal of Geophysical Research*, *102*(C11), 25173–25194. https://doi.org/10.1029/97jc00445

Simmons, H. L., Hallberg, R. W., & Arbic, B. K. (2004). Internal wave generation in a global baroclinic tide model. *Deep Sea Research Part II: Topical Studies in Oceanography*, *51*(25–26), 3043–3068. https://doi.org/10.1016/j.dsr2.2004.09.015

Spicer, P., Huguenard, K., Ross, L., & Rickard, L. N. (2019). High-frequency tide-surge-river interaction in estuaries: Causes and implications for coastal flooding. *Journal of Geophysical Research: Oceans*, *124*(12), 9517–9530. https://doi.org/10.1029/2019jc015466

Stammer, D., Ray, R. D., Andersen, O. B., Arbic, B. K., Bosch, W., Carrère, L., et al. (2014). Accuracy assessment of global barotropic ocean tide models. *Reviews of Geophysics*, *52*(3), 243–282. https://doi.org/10.1002/2014rg000450

Stepanov, V. N., & Hughes, C. W. (2004). Parameterization of ocean self-attraction and loading in numerical models of the ocean circulation. *Journal of Geophysical Research*, *109*(C3). https://doi.org/10.1029/2003jc002034

Tozer, B., Sandwell, D. T., Smith, W. H. F., Olson, C., Beale, J. R., & Wessel, P. (2019). Global Bathymetry and topography at 15 arc sec: SRTM15+. *Earth and Space Science*, *6*(10), 1847–1864. https://doi.org/10.1029/2019EA000658

Van der Walt, S., Schönberger, J. L., Nunez-Iglesias, J., Boulogne, F., Warner, J. D., Yager, N., et al. (2014). Scikit-image: Image processing in Python. *PeerJ*, *2*, e453. https://doi.org/10.7717/peerj.453

Vinogradova, N. T., Ponte, R. M., Quinn, K. J., Tamisiea, M. E., Campin, J.-M., & Davis, J. L. (2015). Dynamic adjustment of the ocean circulation to self-attraction and loading effects. *Journal of Physical Oceanography*, *45*(3), 678–689. https://doi.org/10.1175/jpo-d-14-0150.1

Von Kármán, T. (1931). *Mechanical similitude and turbulence (No. 611)*. National Advisory Committee for Aeronautics. Retrieved from https://resolver.caltech.edu/CaltechAUTHORS:20140804-121813080

Wang, H., Xiang, L., Jia, L., Jiang, L., Wang, Z., Hu, B., & Gao, P. (2012). Load Love numbers and Green's functions for elastic Earth models PREM, iasp91, ak135, and modified models with refined crustal structure from Crust 2.0. *Computers & Geosciences*, *49*, 190–199. https://doi.org/10.1016/j.cageo.2012.06.022

Waterhouse, A. F., MacKinnon, J. A., Nash, J. D., Alford, M. H., Kunze, E., Simmons, H. L., et al. (2014). Global patterns of diapycnal mixing from measurements of the turbulent dissipation rate. *Journal of Physical Oceanography*, *44*(7), 1854–1872. https://doi.org/10.1175/jpo-d-13-0104.1

Williams, M. J., Jenkins, A., & Determann, J. (1985). Physical controls on ocean circulation beneath ice shelves revealed by numerical models. In *Ocean, ice, and atmosphere: Interactions at the Antarctic Continental Margin* (Vol. *75*, pp. 285–299). https://doi.org/10.1029/ar075p0285